Cold Regions Science and Technology 146 (2018) 155–166

Contents lists available at ScienceDirect

Cold Regions Science and Technology

journal homepage: www.elsevier.com/locate/coldregions

Analyzing the oscillations of the Perito Moreno Glacier, using time-lapse image sequences

María G. Lenzano[a,*], Esteban Lannutti[a], Charles Toth[b], Luis Lenzano[a], Andrés Lo Vecchio[a], Daniel Falaschi[a], Alberto Vich[a]

[a] Departamento de Geomática, Instituto Argentino de Nivología, Glaciología y Ciencias Ambientales, CONICET, Mendoza, Argentina
[b] Department of Civil, Environmental and Geodetic Engineering, The Ohio State University, OH, USA

ARTICLE INFO

Keywords:
Time-lapse imagery
Ice-dammed
Glacier dynamics
Perito Moreno

ABSTRACT

In this study, we analyze the dynamic process of ice-dam formation by the Glaciar Perito Moreno (GPM), located on the Argentinean side of the southern tip of South America. When this glacier advances through the waters Lago Argentino and reaches the Península de Magallanes (PM), it has been regularly producing an ice-dam between the Brazo Rico (BR) and Canal de los Témpanos (CT-LA) since the early twentieth century; the last registered episode was in February 2016. Using the Advance-Close-Open-Retreat (ACOR) concept, we analyze the oscillation cycle of GPM, the feedback mechanism. From limnimetric scales observations during the 1994–2015 time period, it can be demonstrated that GPM exhibits different behaviors during the charge and discharge processes, classified by three types of outburst: sudden, progressive, and minor. The maximum discharge rate of a sudden event goes up to 8000 $m^3 s^{-1}$, while a minor event may be as low as 123 $m^3 s^{-1}$. To obtain detailed shape information of ice-dam formation at high temporal resolution, daily time-lapse images were acquired by two professional DSLR cameras from April 2012 to April 2013. The daily data allows for accurate estimation of the position and its rate of change in the terminus area of the glacier where the ice-dam develops, including the estimation of the height and width of the drainage tunnel forming at the base of the ice-dam. The glacier is advancing between June and December, and retreating between December and April. Based on the time-lapse image measurements, the forward and retreat motion of the glacier was estimated to be 0.53 m day^{-1} and -1.1 m day^{-1} with an estimation error of $\pm$ 0.04 m day^{-1} between April to October (2012) and January and April (2013), respectively. The seasonal variation in the position of the glacier was found to be $\pm$ 65 m in this period. The results obtained by the methods and techniques implemented have clearly demonstrate that the annual advance of the glacier front typically leads to an ice-dam formation, which is a complex process, and there is a feedback mechanism between GPM and LA that primarily controls the oscillations of the glacier front around the otherwise quite stable position.

1. Introduction

Numerous types of dams can be formed by natural processes, such as landslides, glacial ice and late-neoglacial moraines (Costa and Schuster, 1988). Glacial outburst floods may result from the failure of ice-dams (Westoby et al., 2014). Ice-dammed lakes can cause considerable geomorphologic changes in glacial environments because of the repeated or irregular release of the water stored within them (Tweed and Russell, 1999), and eventually have a potential hazard to downstream environments (Jacquet et al., 2017). Sometimes, the origin of ice dams in the margin or terminus of a glacier is linked to glacier front advances (Björnsson, 1998). The frequency of these events may increase along with larger magnitude if the atmospheric temperature rises (Iribarren Anacona et al., 2015). To understand the complex ice-dam evolution, the relation between the glacier morphology, terrain and runoff sources are important (Hewitt and Liu, 2010). The characteristics of outburst floods, and the deposits and landforms they produce, depend on the dam failure process, the rate and duration of flow out of the lake, and downstream interactions with sediment and the valley floor (Clague and O'Connor, 2015). Ice-dammed failures are complicated phenomena, driven by different factors, and may often occur periodically with a period of 1 to > 10 years (Costa and Schuster,

* Corresponding author.
E-mail addresses: mlenzano@mendoza-conicet.gob.ar (M.G. Lenzano), elannutti@mendoza-conicet.gob.ar (E. Lannutti), toth.2@osu.edu (C. Toth), llenzano@mendoza-conicet.gob.ar (L. Lenzano), anlovecchio@mendoza-conicet.gob.ar (A. Lo Vecchio), dfalaschi@mendoza-conicet.gob.ar (D. Falaschi), avich@mendoza-conicet.gob.ar (A. Vich).

https://doi.org/10.1016/j.coldregions.2017.11.015
Received 6 September 2017; Accepted 21 November 2017
Available online 05 December 2017
0165-232X/

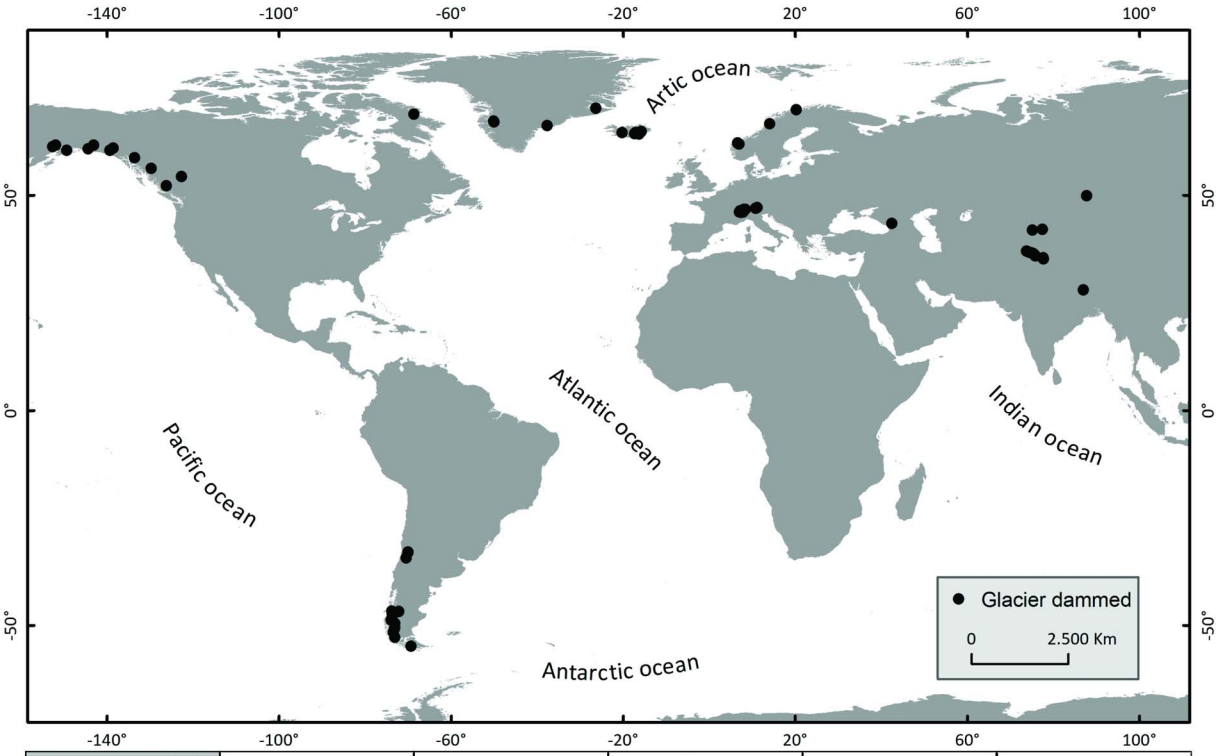

South America (14)	Tempano	Van cleve	Graenalón	Strupvatnet	Khurdopin
Alemania	Viedma	Greenland (4)	Grubengletscher	Trient	Kichik Khumdom
Bonita	North America (11)	Nordbogletscher	Hagavatn	Unter Grindelwald	Lhotse
Cachapoal	Chakachamna	Russell	Kaldakvisl	Vatnsdalslon	Malangutti
Cachet II	Ekalugad	Sondre Stromfjord	Kichik Khumdom	Vernagtferner	Mertsbakher
Dickson	Hidden creek	Sydgletscher	Koldevatn	Zmutt	Shimshal
Gran campo nevado	Hubbard	Europe (25)	Lac de Rochemelon	Asia (15)	Shyok
Grande del Plomo	Kaskawulsh	Crete-Seche	Marjelensee	Abdukagor	Yashkuk Yaz
Hernando Lamero	Snow river	Demmevatn	Orny	Batura	Zyndan
Juncal sur	Strandiline	Findelen	Osterdalsisen	Biafo	
Perito Moreno	Strohn	Giétro	Plan Névé	Chong Kumdan	
San Rafael	Summit	Gjánúpsvatn	Rhone	Elbrus	
Steffen	Tulsequah lake	Gornersee	Saleinaz	Karambar	
TOTAL: 69					

Fig. 1. World map of ice-dammed areas; the listing is organized by regions in alphabetic order.

1988).

There are many glaciers whose advance produces the damming of lakes around the world, each one of them displaying different characteristics; most of them are located in the Northern Hemisphere. Fig. 1 shows a global inventory of ice-dammed lakes, containing a total of 69 glaciers (Hewitt, 1982; Haeberli, 1983; Walder and Costa, 1996; Narama et al., 2010; Vincent et al., 2010; Margold et al., 2011; Loriaux and Casassa, 2013; Fitzpatrick et al., 2014; Iribarren Anacona et al., 2015; Lo Vecchio et al., in review). 60% of the identified glaciers are located in maritime environments, and their fronts are in direct contact with seawater and/or proglacial lake. These glaciers are mostly found at latitudes higher than 50°, such as the Patagonian Andes, Western Canada, Southern Alaska, the peninsular area of Northeastern Canada, Greenland, Iceland and the northern region of Norway. The rest of the glaciers are in continental environments, near mountain ranges, such as the Andes, the Alps, and the Himalayas. In the Central Andes of Argentina, the Nevado del Plomo has produced enormous damage to human settlements and infrastructure due to the failure of a glacier lake formed after a glacier surge in the XXth century (Bruce et al., 1987; Fernández et al., 1985; Leiva et al., 1989; Fernández et al., 1991; Harrison et al., 2015). On the Argentinean side of the Southern Patagonia Ice field, the Glaciar Perito Moreno (GPM) is an outlet glacier, been observed since 1897 (Aniya and Skvarca, 1992), has undergone numerous collapses since the early twentieth century, and, when the GPM abuts the Peninsula de Magallanes (PM), an ice-dammed lake is produced. The last of these episodes took place on March 12, 2016 when a new rupture of the ice-dam at the Peninsula de Magallanes occurred. The GPM, resting on its bedrock, generates front oscillations, leading to recurrent cycles of advance, closure, damming, flood, failure and subsequent retreat of the glacier front (Sersic, 1988). The glacier begins to retreat in early summer (typically in December) and then turns to advance in mid-autumn (typically in April) (Minowa et al., 2017). Over the past decade (Minowa et al., 2015), GPM has shown short-term advances and retreats, though the mechanisms of the seasonal variation is not yet understood (Minowa et al., 2017). Numerous studies have been conducted on GPM, mostly focussing on surface velocities, geophysical investigations and mass balance at the terminal part during the last decades (Rott et al., 1988; Skvarca, 2002; Aniya et al., 2007; Stuefer et al., 2007; Ciappa et al. 2010; Sugiyama et al., 2011; Minowa et al., 2015; Minowa et al., 2017, etc.). However, little is currently known about the triggering factors and mechanisms at the ice-dam or understanding the seasonal cyclic oscillations (Sersic, 1988; Skvarca and Naruse, 1997; Skvarca and Naruse, 2005; Pasquini and Depetris, 2011; Minowa, 2017). The range of topographic settings, in

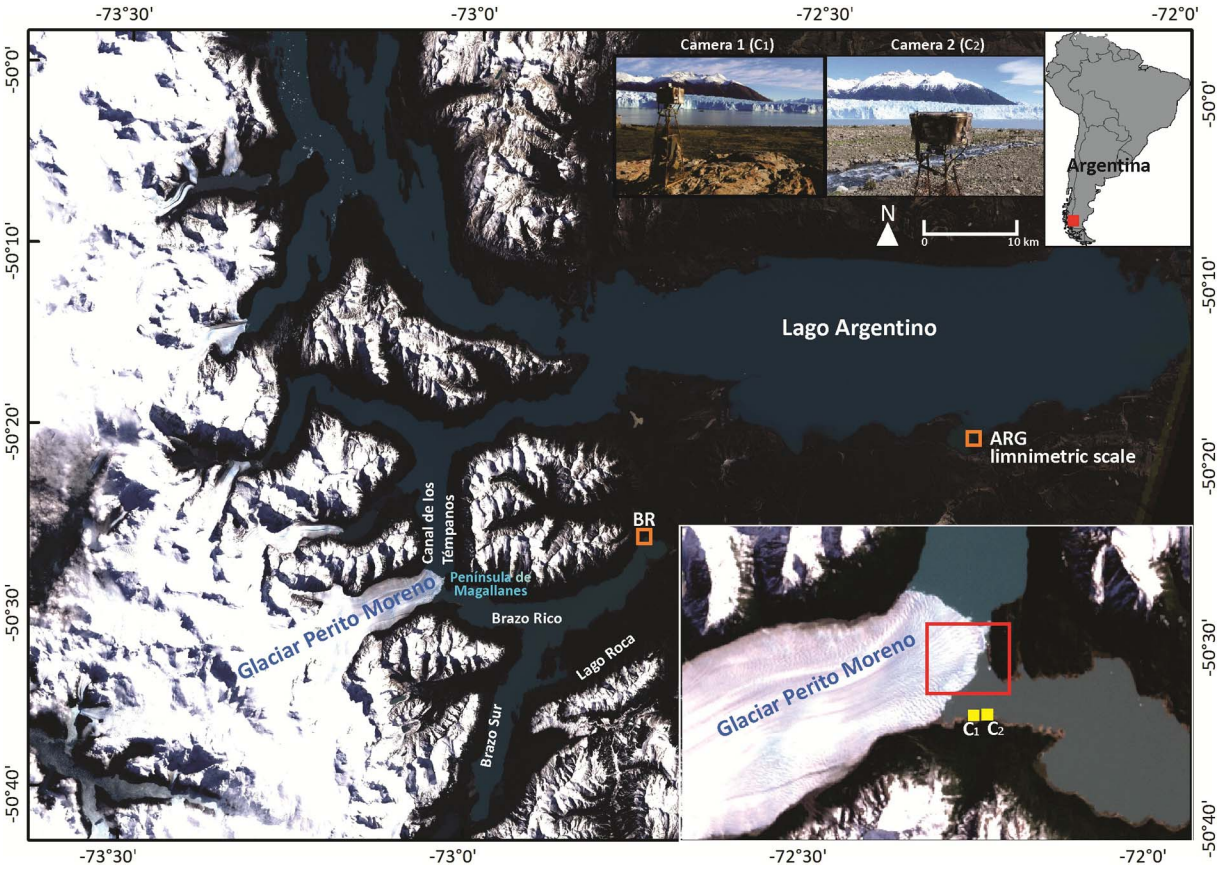

Fig. 2. Map of the study area; the detail map shows the camera locations (C_1 and C_2) with the observed area (red square). (For interpretation of the references to color in this figure legend, the reader is referred to the web version of this article.)

which general type of ice-dammed lakes can be found, identifying the type of lake and the likely flood routing, are given by Tweed and Russell (1999), providing a basis for discussion of the controls on the ice-dam characteristics, including outlet type, tunnel, peak discharge, hydrograph type, etc., The advance of the GPM into an existing water body, however, is an exception to the general classification (Walder and Costa, 1996), though it is not conceptually different. For this reason, it is relevant to improve our understanding by studying the GPM.

Reliable measurements for ice-dam monitoring require the use of data acquisition techniques with an adequate spatial and temporal resolution to cover the dynamics of the changes. Regrettably, glaciers are usually located in geographically complex and hard to access areas with challenging weather conditions. Optical sensors on satellite platforms may often have limitations to observe terrain in mountain regions (Gleitsmann and Kappas, 2006), such as the Southern Patagonian Andes where cloud cover is particularly persistent. Therefore, using ground and near ground platform based remote sensing, a rapidly advancing technology, mainly driven by imaging sensor developments (Toth and Jóźków, 2016), represents an attractive approach to study these areas. A wide range of digital cameras can easily acquire high-resolution images, and then using terrestrial digital photogrammetry (TDP) technique (Pitkänen and Kajuutti, 2004) accurate geospatial information can be extracted. TDP methods enable data analysis from a different perspective compared to data provided by airborne remote sensing methods (Gance et al., 2014), and offers a potentially rapid, useful and complementary research tool for deriving surface roughness metrics over space and time at scales critical to the dynamics of the glacier and ice-dam (Irvine-Fynn et al., 2014). Techniques using non-metric cameras for spatial measurement have become well established, with many notable contributions to the development of analytical photogrammetric methods in the 1980s (Chandler et al., 2005). In addition, the application of accurate time-lapse (TL) imagery with calibration is of great interest to study glaciers since it provides the temporal and spatial resolution needed to adequately detect glacier changes. Both, monoscopic and stereoscopic TDP methods have been successfully used in glaciological applications since the 90s (e.g. Harrison et al., 1992; Hashimoto et al., 2009; Ahn and Box, 2010; Svanem, 2010; Maas et al., 2010; Rivera et al., 2012; Danielson and Sharp, 2013; Lenzano et al., in press).

The main objective of this study is to analyze the oscillation cycle of the GPM glacier, characterized by the Advance-Close-Open-Retreat (ACOR hereafter) processes. The investigation is based on processing two datasets with specific methods. The first one is the TDP processing of stereoscopic TL images, acquired by non-metric professional DSLR camera systems, daily from April 2012 to April 2013, capturing the evolution of an ice-dam (tunnel formation) and its collapse on January 19, 2013. This allowed deriving daily data of front positions and velocities in the ice-dammed area, including the height of the calving front above lake level and tunnel dimensions. The second data stream, provided by lake level measurements of Brazo Rico (BR) and Lago Argentino (LA) from 1995 to 2015 characterizes the charge and discharge processes, which are essential to analyze the interaction of GPM and PM. Combining both datasets provides a strong base to understand the oscillatory behavior of GPM.

2. Area description and history of ice-damming

The Southern Patagonian Ice field (SPI) is located at the border of Argentina and Chile in the southern tip of South America. It covers an area of 13,000 km^2 and glaciers have an average length of approximately 30–40 km; the mean altitude is 1191 m ASL (Aniya, 2013). Presently, it is the third largest reservoir of fresh water on land after

Table 1
Ice-dammed events and studies of Glacier Perito Moreno.
The table is modified from Stuefer (1999).

Date of damming	Rupture date	Discharge date	Damming height (m)	Source
1917	1917	–	–	Liss, 1970
1934/35	1934/35	–	–	Liss, 1970
(Austral) winter 1939	February 17, 1940	–	10.5	Liss, 1970
(Austral) winter 1941	March 21, 1942	–	14.9	Liss, 1970
December 1946	–	–	–	Aniya et al., 1992
(Austral) winter 1947	(Austral) spring 1947	–	2.6	Liss, 1970
November 1947	–	–	–	Aniya et al., 1992
April–December 1948	–	–	–	Aniya et al., 1992
July 1951	March 2, 1952	–	12.7 (11.3[b])	Liss, 1970
September 1952	March 30, 1953	–	14.4 (12.8[b])	Liss, 1970
July 1954	September 14, 1956	–	26.7 (26[b])	Liss, 1970
	October 10, 1956[a]		25.6	
August 1959	February 15, 1960	–	13.1	Liss, 1970
	March 31, 1960[a]		11.6	
September 1962	February 25, 1963	–	15.7	Liss, 1970
August 1964	February 10, 1966	–	28.4	Liss, 1970
	February 25, 1966[a]		27 approx.	
–	1970	–	–	Stuefer, 1999
–	1972	–	–	Stuefer, 1999
–	1975	–	–	Stuefer, 1999
–	1977	–	–	Stuefer, 1999
–	1980	–	–	Stuefer, 1999
–	1984	–	–	Stuefer, 1999
–	February 17, 1988	–	–	Stuefer, 1999
October 1, 2003	March 14, 2004	March 11, 2004	9.35	Skvarca and Naruse, 2005
	March 13, 2006	March 10, 2006	–	Stuefer et al., 2007
August 1, 2005			5.4	Present study
	July 9, 2008		–	Pasquini and Depetris, 2011
August 3, 2007		July 4, 2008	8.1	Present study
November 5, 2011	March 4, 2012	February 29, 2012	5.8	Present study
October 1, 2012	January 19, 2013	November 21, 2012	2.4	Present study
September 10, 2013	December 30, 2013	December 18, 2013	3.7	Present study
October 26, 2015	March 10, 2016	March 10, 2016	8.4	Present study

[a] 2nd rupture.
[b] Heinsheimer 1958 (after Raffo, Colqui and Madejski).

Antarctica and Greenland. The Glaciar Perito Moreno is located at 50°28′ S, 73°02′ W, within the Los Glaciares National Park, in the province of Santa Cruz, Argentina. This is an important calving glacier in the region due to its size and its unusual behavior exhibited by only minor fluctuations of the glacier front for about 80 years, when most of the SPI glaciers have retreated during the last 50 years (Stuefer et al., 2007). When perched against the Magallanes Península, the terminus of GPM divides Lago Argentino into the Canal de los Témpanos to the north, and Brazo Rico to the southeast, see Fig. 2.

The GPM has registered numerous front advances at irregular intervals since the end of the nineteenth century. Since then, the glacier front has repeatedly fluctuated by hundreds of meters, though not suffering large changes (Stuefer, 1999). Between 1934 and 1988 the events were frequent and also increased their magnitude with each closure. During fifteen years, until 2003, no events were registered, while six episodes have occurred since then. The last event was registered on March 2016. Table 1 shows the timing of damming, rupture and discharge date of GPM from 1917 to present, according to various authors (see also Section 3.2 and Fig. 6).

3. Data collection

3.1. Camera system

To support the field acquisition of time-lapse images, two cameras suitable for field deployment and digital photogrammetry applications (Chandler et al., 2005) were selected. One integrated data acquisition system was built around the CANON EOS Mark II DSLR camera (C_2); pixel size: 7.2 μ, objective focal length: 50 mm; and FOV: 46°. Prior to field installation, the C_2 was calibrated, initially by the United States Geological Survey (USGS), and then prior to field deployment. The second system was based on a NIKON D3 camera (C_1), calibrated by Rollei metric; pixel size: 8.5 μ, objective focal length: 35 mm; and FOV: 62°. The cameras were installed 165 m far from each other to achieve the stereoscopic sensor geometry. The systems are powered by 12 V/7 Ah lead acid batteries, charged by two 38 W solar panels for each camera. The cameras with the supporting electronic systems are protected by a waterproof enclosure. An inspection port in the rear of the enclosure provides visual access to the camera status display. The image acquisition systems were installed on rigid metal structures, fixed to rock outcrops of the shoreline of Brazo Rico, at the terminus of GPM. The location of the cameras, chosen in accordance with National Park requirements, provides a good side view of PM, see Fig. 2. The data acquisition of both systems started on April 17, 2012 and lasted until April 5, 2013. Note that the systems were not able to work properly for 19 days due to adverse climatic conditions during June and July of 2012. Images for a total of 352 days were captured at 11 am, when the Sun has the highest position, in order to minimize errors due to varying illumination angles (Gance et al., 2014). In addition, during the summer season, January–March in the Southern Hemisphere, images were also taken at 10 pm local time because of the longer sunlight interval during these months.

In addition, the relative and absolute orientation of the cameras was performed by conventional surveying measurements using total station. First, the cameras were leveled, making the image sensor vertically positioned and the optical axis horizontal. Then, both camera were oriented towards north, with a final azimuth of 90°19′02″, see Fig. 4, in order to facilitate the photogrammetric processing. Finally, the projection center of the cameras was determined by GPS measurements; WGS coordinates were converted to a local mapping frame (C_1:

6075.47 m N-S; 6289.43 m W-E; 216.38 m H; C_2: 6076.39 m N-S; 6123.33 m W-E; 215.81 m H).

3.2. Lake level measurements

The time series of daily limnimetric scales of heights at Lago Argentino and Brazo Rico from 1994 to 2015 were obtained from Argentina's Subsecretaría de Recursos Hídricos de la Nación record, see Fig. 6.

3.3. Satellite images

Landsat images were used to map the outlines of Brazo Rico (BR), Brazo Sur (BS) and Lago Roca (LR) from 2000 to 2015. The images were selected according to their availability in the Glovis data poll archive (https://glovis.usgs.gov/), resulting in a total of 19 images adequate for processing. The lake areas were manually digitized (Nuth et al., 2013); the horizontal average error was 1.1 pixels per coordinate. The maximum error in area estimation was 4.4 km^2, representing < 5% of the total area. The water body outlines were used to characterize the hydrological processes and the discharge from BR to CT due to the GPM ice-damming, discussed in Section 4.2.

4. Geospatial data processing and analytical ice-dammed behavior

The main processing workflow is shown in Fig. 3; all the algorithms and data handling processes were implemented in Matlab. The input datasets include the DSLR camera images, measurements of BRL (Brazo Rico Level), LAL (Lago Argentino Level), and a reference value (RV), to adjust both height levels, and Landsat satellite images. The overall procedure is divided into camera data processing and charge-discharge analytical assessment. The first one is the stereo photogrammetric processing of the time-lapse image sequences from April 2012 to April 2013. The stereo technique was partially validated by comparing the results to results obtained from a monoscopic camera processing; for more details, see Lenzano et al. (2014). The final results of the time-lapse image processing provide the glaciological dynamics for the area, including the movements and behavior of the glacier terminus. In parallel, the measurements of lake levels and the satellite images were used to estimate the difference of the height level between BR and CT, and the rate of discharge, visualized by hydrograph for the 1995–2015 period. Finally, combining the results from processing thread, a concept (ACOR) was developed to characterize the GPM oscillation.

4.1. Stereo processing of images sequences

The fixed stereo configuration of the cameras and their known exterior orientation make the photogrammetric processing fairly straightforward. Furthermore, the alignment of the cameras provides very favorable condition for 3D point extraction, as the depth changes along the horizontal axis of the stereo model. The image acquisition was synchronized accurately enough with respect to the dynamics in the observation place, so motion artifact exists. During the processing 3D object points are extracted by manual measurements. The computation is based on ray intersection, lines of sight from both cameras, C_1 and C_2, by identifying the same location on the ice. The approximate location of a point could be computed, as illustrated in Fig. 4. The intersection point P projected onto the focal plane of the any camera, P′, say for camera C_2, can be described by image coordinates, see for example,

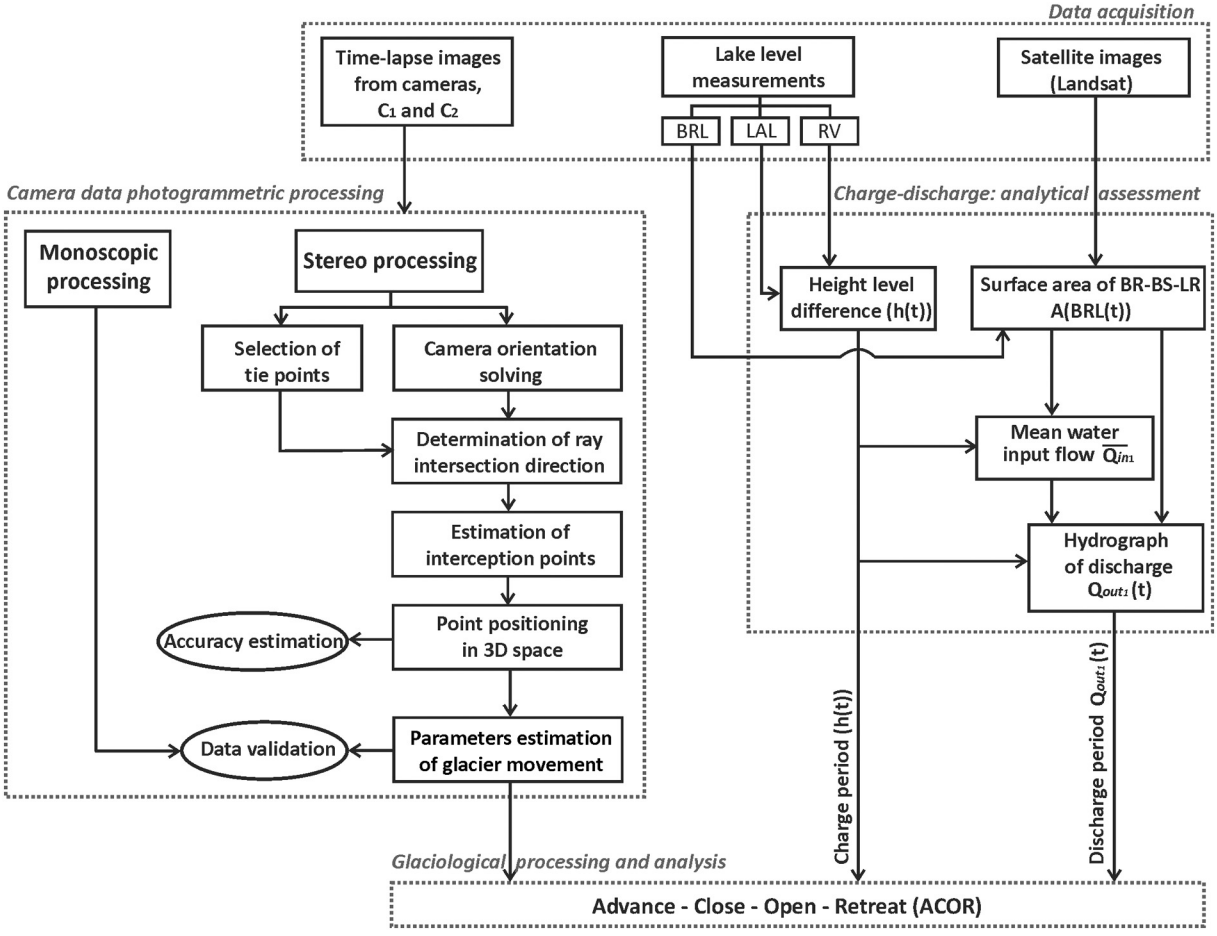

Fig. 3. Workflow of the study.

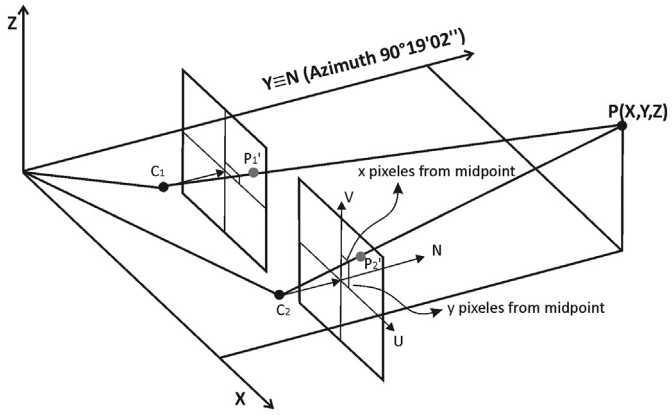

Fig. 4. Stereo camera arrangement.

Corripio (2004) and Rivera et al. (2012), as Eq. (1):

$$\overrightarrow{C_2P_2'} = f\overline{N} + K_x\overline{U} + K_y\overline{V} \quad (1)$$

where: f denotes the focal length, K_x and K_y are the x and y photo coordinates, the number of pixels in the X and Y direction multiplied by the pixel size, respectively. Taking into account the favorable geometrical condition of the cameras, both cameras have the same azimuth and photo coordinate system, the computation is simplified with respect to a generic stereo model. Note that the optical axis points to north, $\overline{N}$, the vectors $\overline{U}$ and $\overline{V}$ sensor axes are parallel, thus $\overline{N} \equiv Y$ (19′02″ offset to the north direction); $\overline{V} \equiv Z$ (nadir direction), and $\overline{U} = \overline{N} \times \overline{V}$. Applying Eq. (1) both cameras, the direction of the intersecting lines, $\hat{u}$ and $\hat{v}$, can be computed as

$$\hat{u} = \frac{\overrightarrow{C_1P_1'}}{\|\overrightarrow{C_1P_1'}\|} \quad (2)$$

$$\hat{v} = \frac{\overrightarrow{C_2P_2'}}{\|\overrightarrow{C_2P_2'}\|} \quad (3)$$

Since the absolute position and orientation of the two cameras are known, it is simple to calculate the 3D coordinates of any point visible on both photographs, using the intersection process. The coordinates of P_1 and P_2 are obtained by calculating the interception of two rays in 3D (Dunn and Parberry, 2002) as

$$t_1 = \frac{[(C_2 - C_1) \times \hat{v}] \bullet (\hat{u} \times \hat{v})}{\|\hat{u} \times \hat{v}\|^2} \quad (4)$$

$$t_2 = \frac{[(C_2 - C_1) \times \hat{u}] \bullet (\hat{u} \times \hat{v})}{\|\hat{u} \times \hat{v}\|^2} \quad (5)$$

$$P_1 = C_1 + t_1\hat{v} \quad (6)$$

$$P_2 = C_2 + t_2\hat{u} \quad (7)$$

where C_1 and C_2 are the known camera positions. The point P (X, Y, Z) in the object space is defined by the positions P_1 and P_2. As the estimated P_1 and P_2 usually produce different coordinate's locations (space intersection), conventionally, the average coordinate is computed using the mean value of Eqs. (6) and (7); though, other methods are available too.

Since the base/height (B/H) ratio is rather small compared to usual photogrammetric practice, multiple resections were performed based on different image measurements, so the 3D positions could be averaged to improve accuracy. The mean GSD at 1600 m was 0.40 m ± 0.03 m. Note that the base was 165 m and the depth ranges between 1000 m and 1600 m. Thus, the estimated accuracy of depth estimation was in the range of 0.30 m and 0.75 m (Chang and Chatterjee, 1992).

4.1.1. Glacier parameter estimation

To model the glacier evolution from April 2012 to April 2013, the key parameters, including frontal positions, velocities, height, and tunnel dimensions, were computed from the stereoscopic data. The front position of GPM was estimated in three areas, P_1, P_2, P_3 (see Fig. 9), in order to analyze the behavior of the front. In addition, the height of GPM at two sites were also evaluated, so the tunnel characteristics, width and height, can be analyzed. Note the stereo camera based results in the tunnel height estimation were also validated by monoscopic, image sequence based results, shown in Fig. 9.

4.2. Charge-discharge process assessment

The oscillatory nature of ice-damming at GPM was analyzed and characterized in terms of the charge and discharge flows for ten years, by estimating the lake level difference between BR and CT (BR − CT h (t)) and the discharge hydrograph (Q_{out1}) of the channel that communicates the water bodies. The selection was based on assessing the events shown in Table 1. Four years were selected between 1994 and 2003 when GPM did not produce an ice-dam (1994, 1995, 1996, 1997). Then six were selected corresponding to years where events with different intensities occurred (2004, 2006, 2008, 2012, 2013a, 2013b).

Fig. 5 shows a schematic of the hydrology-topography-glacier system that is involved in the ACOR oscillation process of GPM. Overall, the system is represented by a water reservoir (R_1) and the correspondent Q_{in1} and Q_{out1} input and output flows. R_1 includes Brazo Rico (BR), Brazo Sur (BR) and Lago Roca (LR) (see Fig. 2). A second reservoir R_2 is represented by Lago Argentino (LA); lake level is LAL and the input and output flows are Q_{in2} and Q_{out2}, respectively. Water levels LA and CT are assumed to be equal. Between R_1 and R_2, GPM may intrude, causing the closure and then opening of the channel that separates them. This channel and its area of discharge (ad) are controlled by the position of the GPM front during the oscillation cycle. The closing of the channel creates a difference h(t) between R_1 and R_2 which impacts the

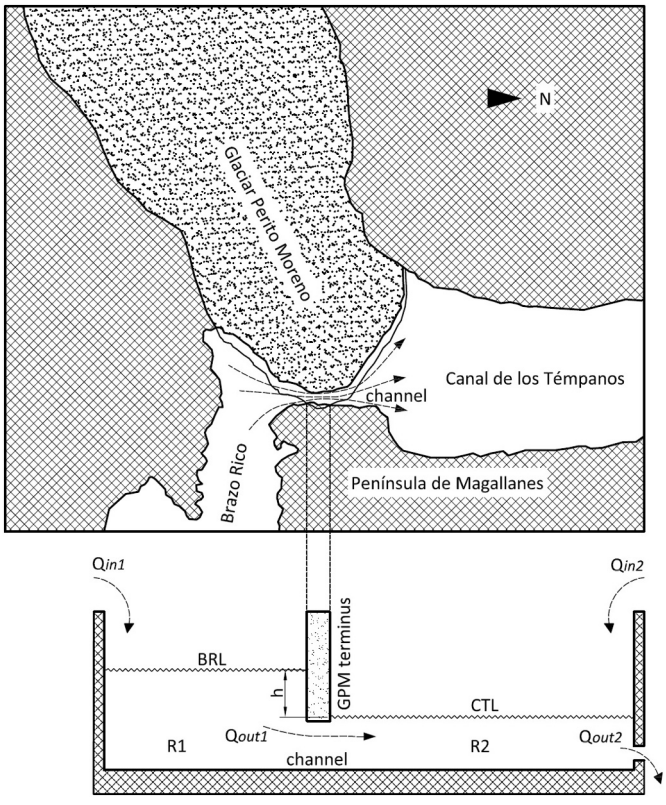

Fig. 5. Schematic graph of the hydrographic system at GPM.

water flow from BR to CT. h(t) and, consequently, Q_{out1}, depend on Q_{in1}, which is the input water flow provided by precipitation and snowmelt entering R_1. On the other side, Q_{in2} represents the water flow input sources entering R_2, including La Leona river and other outlet glaciers calving into LA such as Upsala, whereas Q_{out2} is determined by the Santa Cruz river, which drains LA to the Atlantic Ocean. All of these water inputs and outputs have seasonal variations (Pasquini and Depetris, 2011), though they show a largely integrated impact at the Canal de los Témpanos level (CTL).

4.2.1. Charges cycles

Estimating and characterizing the charge-discharge processes is relevant, since they are defined by the potential energy that accumulates during the approximation and advance of GPM over the PM in the oscillation cycle. This potential energy is mainly determined by the lake level differences between BR and CT. Because the BRL and CTL values are not altimetrically referenced, an adjustment using a reference value RV is needed. Hence, these levels are corrected (RV) based on the elevation difference as measured on December 14, 2003 by Skvarca and Naruse (2005). After the altitudinal adjustment, the lake level difference h(t) can be used to estimate and characterize processes by hydrographs. h(t) is calculated following Eq. (8) as,

$$h(t) = CTL(t) - (BRL(t) + RV) \quad (8)$$

Fig. 6 shows LCT(t), LBR(t), and the level difference h(t) calculated by Eq. (8).

4.2.2. Discharges cycles

From the estimation of the charge processes, the Q_{out1} (hydrograph of discharge) to the CT is obtained. The discharge flow into CT (Q_{out1}) is represented by Eq. (9):

$$Q_{out1}(t) = -A(BRL(t))\frac{dh(t)}{dt} + Q_{in1}(t) \quad (9)$$

where A(BRL(t)) is the area of R_1 which is a function of BRL; obviously, A(BRL(t)) depends on the bathymetry of lake area. This function is approximated by a two degree polynomial, using the R_1 area measurements and the BR lake level (Fig. 7).

Since streamflow in the region has a seasonal variation, a similar trend for Q_{in1} is to be expected. Thus, for the calculation of Q_{in1}, we considered the charge periods when $Q_{out1}(t) \rightarrow 0$, and R_1 and R_2 are disconnected due to the CT closure by GPM. This condition is documented in the ice-damming events registered in 2004, 2006, 2008, 2012, 2013a–b. The mean annual flow $\overline{Q_{in1}}$ was calculated using Eq. (9) and A(LBR(t)) was approximated by a polynomial function, see Fig. 7. Taking into account the temporal match (annual cycle) between h(t) and $\overline{Q_{in1}}$, the discharge hydrographs $Q_{out}(t)$ were calculated for the five charge processes with ice-dammings and two other oscillatory processes with no closure (see Fig. 6). From these results, we classified three types of outburst at GPM: *sudden* and *progressive* (Haeberli, 1983), and *minor*, depending on the magnitude of the potential energy accumulated in the BR and the intensity of the discharge hydrographs.

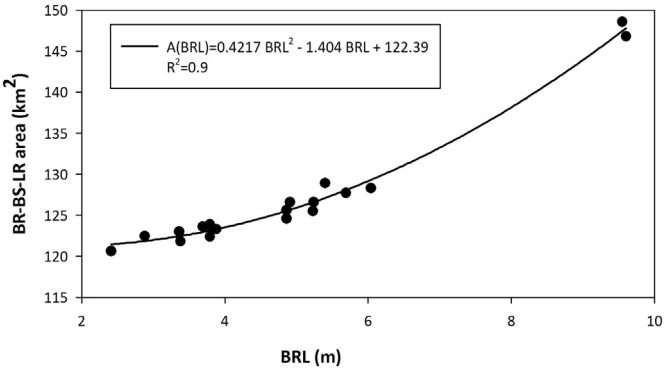

Fig. 7. Approximated A(BRL(t)) as a function of BRL. Note that A(BRL(t)) is the area of R_1, and BRL is the Brazo Rico Level.

5. Results

5.1. GPM movement and derived parameters

5.1.1. Advancing to PM

From the images captured daily, the evolution of the frontal area of GPM at three different positions (P_1, P_2 and P_3) was estimated, as shown in Fig. 8a. Note that point P_3 is defined by the GPM front position at the height of the BR-channel at the intersection of ice, water and air. The elevation changes at the GPM front were also estimated as the glacier reached PM during the 2012–2013 study period, see Fig. 8b. Before April 2012, the glacier front was 111 m away from PM. P_1, P_2 and P_3 all have a similar advancing trends; note that the front of GPM was nearly vertical. From April to October the glacier front moved forward at 0.53 m day^{-1} ± 0.04 m day^{-1} rate. Noteworthy, the glacier front was elevated by 10.3 m (H_2) towards the end of July; mainly, due to the proximity of PM, see Fig. 8b. During the same period, the glacier velocity decelerated from 0.59 m day^{-1} to 0.44 m day^{-1}. The glacier front maintained approximately a constant height, 88 m on average, until November, just before the formation of the tunnel. The annual mean height of the glacier front was estimated at 86 m (H_1) and 71 m (H_2).

5.1.2. Ice-dam formation and persistence

As the GPM front reached PM, P_1, P_2 and P_3 responded differently and the glacier front acquired a convex shape. During the period of tunnel formation, H_1 diminished from 90 m to 76 m.

Formation of the tunnel in the ice-dam started on November 26,

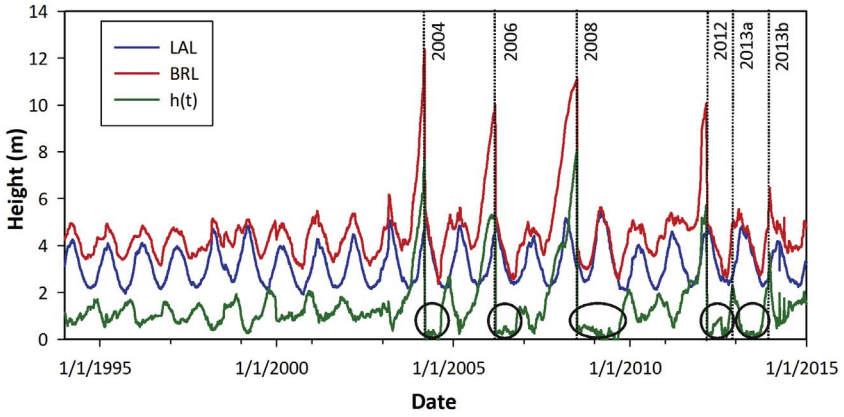

Fig. 6. The time series of daily limnimetric scales of heights at Lago Argentino and Brazo Rico. (For interpretation of the references to color in this figure, the reader is referred to the web version of this article.)

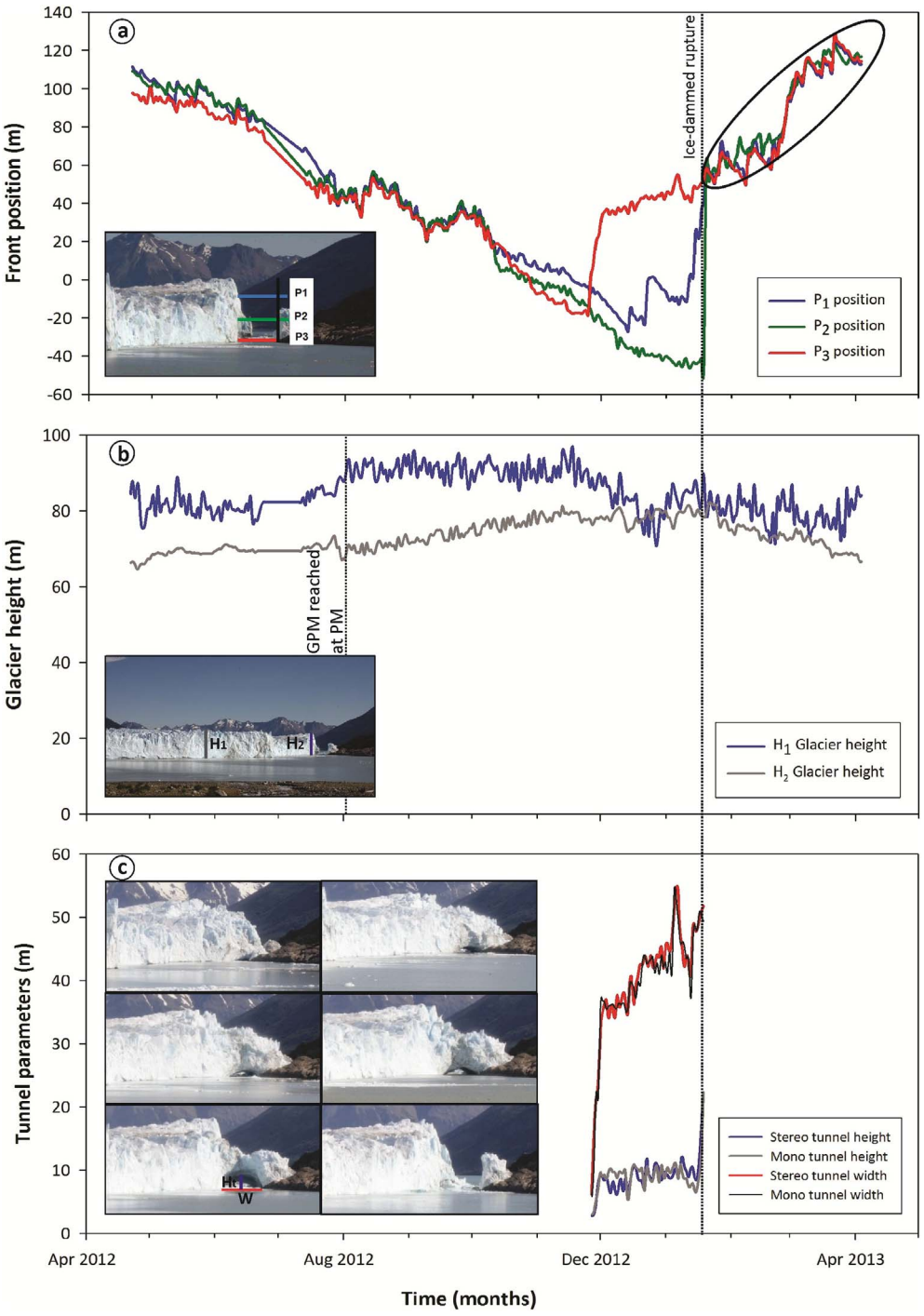

Fig. 8. Parameter estimation results from TL stereo technique (2012–2013 period). a: Front position (P_1, P_2 and P_3), black ellipse indicates the calving process. b: Glacier daily height evolution at front and side. c: Tunnel dimensions during the ice-dam formation, including results of monoscopic processing.

2012. The lake continued to fill up until the date of rupture on January 19, 2013. The width and height of the tunnel were measured and the data is presented in Fig. 8c. The shape of the tunnel was roughly an ellipse. During the tunnel's life, the height increased to a maximum value of 22.3 m, only two days before collapsing. The tunnel width progressively increased to a maximum value of 51.8 m, due to lateral undermining and erosion of the tunnel's interior walls. This was followed by rapid changes in the tunnel geometry until the final collapse event. Interestingly, the glacier front had retreated 52 m immediately after collapse, which represents 50% of the total glacier oscillation. The results of the tunnel evolution, as obtained by stereo camera processing were also compared to the data from the single camera processing (see Lenzano et al., 2014). The *r* Pearson correlation coefficient between both methods was 0.96 (width) and 0.88 (height), showing a good match between time-lapse stereo and single data.

5.1.3. Aperture and retreat

Between January 19 and April 2013, GPM retreated at the mean rate of $-1.1\ \mathrm{m\ day^{-1}}$, twice as fast as the advancing rate. By April 2013, GPM roughly reached the initial position of the previous year, 114 m away from PM. The twice as fast retreat rate with respect to the advance rate is in agreement with the findings of Minowa et al. (2017), who determine advance and retreat velocities of $0.3\ \mathrm{m\ day^{-1}}$ (June–December 2012) and $-0.7\ \mathrm{m\ day^{-1}}$ (December–April 2013) showing similar pattern. It must be noted, however, that the rates determined by Minowa et al. (2017), were surveyed in two different sections of the

GPM front, one of them calving into BR and the other into CT. In contrast, our velocity measurements refer to the ice-dammed channel area that is bounded by both reservoirs. Consequently, the observed discrepancies are likely due to the different data acquisition methods, processing techniques and temporal scales.

After the collapse of the tunnel, the evolution of the GPM front in time shows a highly variable response due to the calving process. Initially, the glacier front tends to advance, which is hampered by the calving process, preventing further advance of the glacier front. This back and forth condition, seen as "peaks" of similar duration in Fig. 8a, marked by black ellipse, eventually gets broken and GPM retreats to its initial position. In April, GPM reaches the initial calving front position that it had the previous year, 114 m from PM. Similarly to the behavior of the GPM front, changes in frontal and lateral height (H_1 and H_2) are also oscillatory, since they also decreased to their initial value in April 2013 after having reached a maximum within the annual cycle. On the other hand, the pattern of the seasonal variations of the glacier front was ± 65 m in the 2012–2013 period according to our study, and ± 80 m in the 1999–2014 period (Minowa et al., 2017); again, it can be partially explained by the use of different data acquisition locations and processing methods.

5.2. ACOR: analytical assessment

According to the topographic characteristics of the site where GPM is located (see Fig. 2), the charge process is closely linked to the shape of the reservoirs (BR-BS-LR) that comprise them, but also the hydrological dynamics of those basins. In addition, another key factor is the GPM interaction with PM and LA.

Drainage can be supraglacial, englacial or ice marginal but is commonly subglacial (Tweed and Russell, 1999), when the hydrostatic pressure of the stored water exceeds the structural capacity of the damming body, or when the stored water is connected to an area of lower hydraulic potential, or when englacial channels are progressively enlarged in an unstable manner, and/or when catastrophic glacier buoyancy occurs (Fountain and Walder, 1998; Richardson and Reynolds, 2000; Gulley and Benn, 2007). When an ice-dam is generated at GPM, the flow of water from BR (R_1) passes through the channel that connects both reservoirs (see Fig. 5), generating a type of subglacial drainage with tunnel formation. According to Tweed and Russell (1999), tunneled drainage tends to be characterized by a prolonged approach of peaking discharge followed by a rapid decrease in flow, and the flooding lasting anywhere from hours to days. In this study, the discharge processes showed different behaviors at GPM.

Fig. 9 shows the various hydrographs: the input flow $Q_{in1}(t)$, discharge $Q_{out1}(t)$, the level difference h(t), and the front position P_3. The P_3 position was selected to characterize the cycles of the front movement, charge and discharge as well as retreat. Analyzing the relationship of these patterns over the full cycle is essential to study the behavior of GPM, including advance in June–December and retreat in April–June.

5.2.1. Progressive outburst of 2013a

Fig. 9a and b shows that the charge process in BR started on September 9, as indicated by the slope change of the h(t) curve, when the GPM front was 30 m away from PM. The charge process reached a maximum level of 2.2 m (green line in Fig. 6) on November 21, which is close to the formation of the tunnel on November 26; note that the latter was directly observed from the TL imagery. Consequently, we can infer that the discharge process started earlier (5 days before) with the formation of a subaqueous tunnel. From that point on, the discharge flow from BR to CT is clearly evident, and is coincident with the formation and break-up of the tunnel and the subsequent glacier front retreat. The discharge process was not fully completed even after the failure of January 19, as evidenced by the TL sequences, where a fully opened channel cannot be observed. The discharge process was progressive and lasted for 85 days. The grey dashed and grey lines in Fig. 9 show the input and output flows Q_{in1} and ($Q_{out1}(t)$), respectively. When ($Q_{out1}(t)$) exceeds Q_{in1} on February 4, the discharge flow reaches a maximum value of 205 $m^3 s^{-1}$. At the beginning of March, the position of the glacier front lies at a distance > 100 m from PM, and the lake levels BRL and LAL tend to pair.

The event at the end of December 2013 (2013b, see Fig. 6) is also considered progressive due to similar characteristics, as the h(t) reached a level of 3.7 m and discharge flow peaked at 220 $m^3 s^{-1}$. The discharge lasted 65 days.

5.2.2. Sudden outburst of 2006

Fig. 9c shows an example of sudden discharge, as on March 10, 2006 the lake level difference between BRL and LAL reached a maximum value of 5.4 m. Three days later, the ice-dam collapsed and the discharge rate got up to 5850 $m^3 s^{-1}$. The discharge period lasted for four days until March 14, when the BRL and LAL lake levels paired.

Similar to the 2006 ice-dam, the 2004, 2008 and 2012 events showed sudden discharge episodes lasting for approximately four days, with the exception of the 2012 event, which lasted for 14 days. The discharge flow peak rates had values of 5000 and 8000 $m^3 s^{-1}$ for the 2004 and 2008 events, respectively, whereas the 2012 event had a peak rate of approximately 2000 $m^3 s^{-1}$. The 2004 ice-dammed event was studied by Skvarca and Naruse (2005), obtaining similar results, and the minor differences observed are related to methodological aspects such as the input flows calculation.

5.2.3. Minor outburst of 1996

Fig. 9d shows the charge-discharge process for periods with small lake level differences (< 1 m). Although this is a period without an ice-dam, GPM was close enough to prevent water from freely passing through the channel between BR and CT. From October, the charge over BR increases until the end of the month, when the discharge process begins. The discharge flow maximum peak occurs at the end of January with a value of 123 $m^3 s^{-1}$. At the beginning of April, h(t) reaches similar values to the start of the charge process as Q_{in1} equals $Q_{out1}(t)$.

Note that the h(t) levels and the discharge rates of 1994, 1995, 1997 present behaviors and magnitudes similar to those analyzed for 1996.

6. Discussion

The formation and persistence of many ice-dammed lakes are strongly linked to glacier oscillations (Tweed and Russell, 1999), which was confirmed by the obtained results here and the subsequent analyses that the front position of GPM shows oscillations with an annual periodicity. The primary control of this behavior is related to the ablation rates at the calving front rather than changes in flow velocity of the glacier. Minowa (2017) showed that the magnitude of the seasonal variation in frontal ablation rates in his study was five times greater than the ice speed. The frontal ablation rate is driven by many processes where the seasonal variation of air and/or lake temperatures are likely to impact the oscillatory behavior, as these variables may influence the calving and/or subaqueous melting rates (Minowa, 2017). From this study, we infer that the frontal ablation rate and the Glaciar Perito Moreno oscillations are primarily driven by water-topographic interaction during the charge and discharge of water due to the PM and LA communication.

According to recorded data at GPM from the beginning of the twentieth century, the frontal position experienced a sustained advance until 1917, when the glacier front reached PM and then acquired a relatively stable behavior, showing slight variations of oscillatory nature (Skvarca and Naruse, 1997) ever since. Therefore, we can define that the GPM front position shows an annual net advance, attributed to the large up-glacier ice flux due to the relatively large accumulation area and the elevated bedrock topography near the glacier front such as

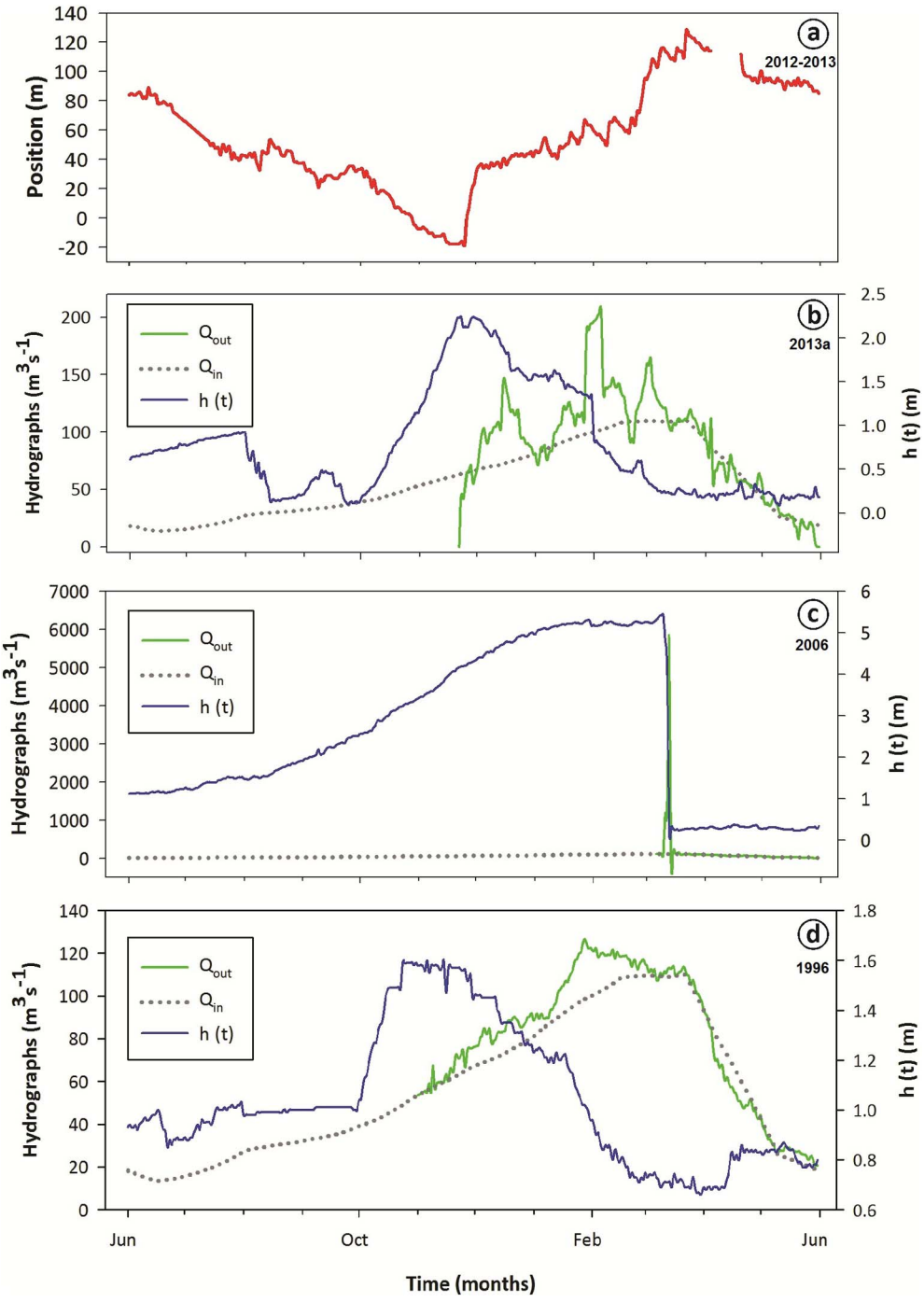

Fig. 9. Hydrographs showing charge and discharge processes of GPM. a: P_3 daily position of GPM during the 2012–2013 period. b: The grey dashed line shows the mean annual flow ($\overline{Q_{in1}}$), $Q_{out1}(t)$ is represented by a green line, h(t) in blue line for the 2013a ice-dammed condition. c: Idem for the 2006 ice-dam. d: Idem for a period without ice-dam (1996). (For interpretation of the references to color in this figure legend, the reader is referred to the web version of this article.)

suggested by Stuefer et al. (2007), Minowa et al. (2015), and Aniya et al. (1992) and Skvarca and Naruse (1997). Nonetheless, this positive advance is held back due to the approaching glacier front to PM and the LA separation through the channel, which defines a natural barrier that controls the front position in an oscillatory process. The narrowing of the channel causes a decrease in the effective area of discharge. Hence, the minimum value of this effective area of discharge will create a lake level difference between BR and CT, defined by the water flow entering to the BR, the lake levels of both reservoirs and the position of the front of the glacier. When GPM advances, and the channel area decreases, the difference between the BR and CT lake levels increases. This increase in potential energy becomes a boost in the discharge water velocity from BR to CT (increased kinetic energy), which raises the ablation rates at the glacier front (Sersic, 1988). Following this process, GPM will approach to PM as long as the balance between the glacier advance and ablation remains positive. The glacier front advance will continue until the water level increase and the narrowing of the channel reach a threshold, beyond which the water velocity increase causes a retreat of the glacier front.

This system, which is driven by the described feedback mechanisms, defines a cyclic approach-charge-discharge-retreat process (ACOR), which, depending on the magnitude of the original net advance, may determine different discharge patterns. If the initial net advance is not strong enough to overcome the retraction caused by the increased ablation before the glacier reaches PM, the glacier front will experience oscillations coinciding with the minimum area of discharge. Examples of this latter case are the variations experienced by the glacier in the 1995, 1996, 1997, 1998, characterized by the lack of ice-dam formation

and an oscillatory fluctuation of the BR-CT levels (amplitude: ~1.1 m, sampling frequency: 365 days^{-1}). On the contrary, if the glacier advance overtakes the ablation during the approach process, a complete closure of the channel occurs and an ice-dam is formed. Once the dam is established, the water flow velocity tends to decrease to zero and the ablation is significantly reduced, favoring the filling of the BR and the future formation of an ice tunnel. As water begins to find it as way under the ice-dam, flow localizes in either a single channel or a small number of channels. The energy dissipated by flowing water melts the surrounding ice, resulting in channel enlargement. As the lake drainage proceeds, water pressure in the channel falls, and ice will creep (which strongly depends on the difference between ice and water pressure) to dominate melting (Walder and Costa, 1996). In this case, the sustained increase in the level of the BR relative to the CT, will end in a process of rupture of the ice reservoir.

The characteristics of the rupture depend on the magnitude of the original net advance at the PM, which, in turn, defines the robustness of the ice-dam. Strong advances with large magnitudes generate robust approaches that can resist great lake level differences between BR and CT. This type of ice-dam culminates in failure processes and sudden discharge flows, characterized by high calving rates and abrupt retreat of the glacier front. Examples of this behavior are the ice-dammed years of 2004, 2006, 2008, 2012, with BR-CT level differences > 5.5 m and flow rates of thousands of $m^3 s^{-1}$, see Fig. 9. The noticeable and sudden increase in the ablation rate makes the glacier retreat to positions further away from the minimum area of discharge, causing BR and CT to level until a new advance overcomes retraction, see Fig. 6, black circles. In addition, there are leading to the ice-dam formation but processes where the magnitude of the net advance is not large enough to generate robust dams. Despite, these processes, when the GPM reaches PM, the formation of ice tunnels occurs. In general, these dams are not robust enough to store sufficient potential energy to generate sudden ruptures. The ice-dams formed during the 2013a and b periods (see Fig. 6), characterized by average BR-CT charge levels (~3 m), formation of an ice tunnel, lower discharge hydrographs (~200 $m^3 s^{-1}$), and important retractions of the front (~120 m) due to the prolonged process of discharge.

In summary, we may conclude that GPM cycle is based on a pattern of ice-dammed lake activity in response to general climate change and local factors such as Evans and Clague (1994) mentioned in other cases, and also may depend on the characteristics of the previous event. This condition would explain the non-periodic stochastic nature of the ice-dam formation and rupture events over time, as shown in Table 1. The magnitude and frequency of outbursts can be effectively linked to the phases of the outburst cycle (Tweed and Russell, 1999). As glaciers recede, ice-dams become thinner resulting in progressively decreasing lake levels, resulting in less water required to initiate an outburst flood (Costa and Schuster, 1988; Evans and Clague, 1994; Clague and Evans, 1997). The magnitude of the GPM front advance has an annual periodicity component associated with seasonal processes such as air and lake temperature, melting, lake level, incoming flows, etc., that are independent from glacier interaction with PM and LA. Nevertheless, the annual net advance of the glacier front leads to a recurrent approach to the PM, where the greatest influence on this process is provided by the austral winter, when the seasonal component presents the most advance positive value. When PM and LA are included in this complex process, a feedback mechanism is formed, which has the primary control of the oscillations around the stable position. The system is driven by the charge and discharge processes of BR, where the annual oscillation cycle is synchronized by the advance phase (June–December), and the retreat phase (December–April), respectively.

7. Conclusions

In this study, the feasibility of time lapse terrestrial photogrammetry for glaciological applications was demonstrated. The proposed technique is cost effective, and the simple data acquisition and subsequent processing provide adequate spatial/temporal resolution to monitor glaciers. The technique was correlated and validated in the changes of the tunnel geometry was compared to a monoscopic photogrammetric method, resulting in a Pearson coefficients of 0.96 and 0.88 for width and height, respectively, indicating a good match between the estimated parameters.

The results from time-lapse technique have shown acceptable quality and accuracy estimation of the geometric parameters of the glacier terminus in the 2012–2013 period. The analysis of daily velocities suggests that Glaciar Perito Moreno moves forward from April to November/December with a velocity rate of 0.53 m day^{-1}, and after that the glacier starts to move back (retreat process) until April reaching −1.1 m day^{-1}, completing a cycle. The amplitude of this oscillation is approximately ± 65 m.

The ACOR analytical assessment at Glaciar Perito Moreno for the 1995–2015 period provided good information to classify three types of outburst: sudden, progressive, and minor. The potential energy accumulated in the charge process is transformed into kinetic energy in the discharge process due to the circulation of the water through the channel, which has the primary control over the front retreat with a noticeable increment of the calving rate. The outburst characteristics define the intensity of net advance of the glacier for a given year, and it is controlled by non-seasonal variables that may be dependent on the climate and the characteristic of the channel closure of the previous year. This may explain the aperiodic nature of ice-dammed events.

In summary, we may conclude that the Glaciar Perito Moreno shows a seasonal oscillatory cycle, controlled by the interaction of the glacier front with Península de Magallanes and Lago Argentino, creating a feedback mechanism of advance, close, open and retreat. The oscillation phase is impacted by advances from the winter (southern hemisphere), related to the seasonality of ablation processes, such as water and air temperature, etc.

Acknowledgments

Fieldwork was funded by grant PICT 1995-2013, Agencia Nacional de Ciencia y Tecnología Argentina (ANCyT). We thank to Los Glaciares National Park for permits to explore the study area and Hielo & Aventura Expeditions for navigation and transportation of personnel and equipment. The authors would like to thank Adalberto Ferlito. Hugo Videla, and Pedro Skvarca for field assistance.

References

Ahn, Y., Box, J.E., 2010. Instruments and methods. Glacier velocities from time-lapse photos: technique development and first results from the Extreme Ice Survey Greenland. J. Glaciol. 56, 198.
Aniya, M., 2013. Holocene glaciations of Hielo Patagónico (Patagonia Icefield), South America: a brief review. Geochem. J. 47 (2), 97–105.
Aniya, M., Skvarca, P., 1992. Characteristics and variations of Upsala and Moreno glaciers, southern Patagonia. Bull. Glacier Res. 10, 39–53.
Aniya, M., Naruse, R., Shizukuishi, M., Skva rca, P., Casassa, G., 1992. Monitoring recent glacier variations in the southern Patagonia icefield, utilizing remote sensing data. Int. Arch. Photogramm. Remote. Sens. 29 (B7), 87–94.
Aniya, M., Enomoto, H., AokiI, T., Matsumoto, T., Skvarca, P., et al., 2007. Glaciological and geomorphological studies at Glaciar Exploradores, Hielo Patagonico Norte, and Glaciar Perito Moreno, Hielo Patagonico Sur, South America during 2003-2005 (GRPP03-05). Bull. Glaciol. Res. 24, 95–107.
Björnsson, H., 1998. Hydrological characteristics of the drainage system beneath a surging glacier. Nature 395 (6704), 771.
Bruce, R.H., Cabrera, G.A., Leiva, J.C., Lenzano, L.E., 1987. The 1985 surge and ice dam of Glaciar Grande del Nevado del Plomo, Argentina. J. Glaciol. 33 (113), 131–132.
Chandler, J.H., Fryer, J.G., Jack, A., 2005. Metric capabilities of low cost digital cameras for close range surface measurement. Photogramm. Rec. 20 (109), 12–26.
Chang, C., Chatterjee, S., 1992. Quantization error analysis in stereo vision. In: Signals, Systems and Computers, October, 1992 Conference Record of the Twenty-Sixth Asilomar, IEEE, Conference on, pp. 1037–1041.
Ciappa, A., Pietranera, L., Battazza, F., 2010. Perito Moreno Glacier (Argentina) flow estimation by COSMO SkyMed sequence of high-resolution SAR-X imagery. Remote Sens. Environ. 114 (9), 2088–2096.
Clague, J.J., Evans, S.G., 1997. The 1994 jökulhlaup at Farrow Creek, British Columbia,

Canada. Geomorphology 19 (1–2), 77–87.
Clague, J.J., O'Connor, J.E., 2015. Glacier-related outburst floods. In: Haeberli, W., Whiteman, C. (Eds.), Snow and Ice-related Hazards, Risks and Disasters. Elsevier, pp. 487–519.
Corripio, J.G., 2004. Snow surface albedo estimation using terrestrial photography. Int. J. Remote Sens. 25 (24), 5705–5729.
Costa, J.E., Schuster, R.L., 1988. The formation and failure of natural dams. Geol. Soc. Am. Bull. 100 (7), 1054–1068.
Danielson, B., Sharp, M., 2013. Development and application of a time-lapse photograph analysis method to investigate the link between tidewater glacier flow variations and supraglacial lake drainage events. J. Glaciol. 59, 287–302.
Dunn, F., Parberry, I., 2002. 3D Math Primer for Graphics and Game Development. Wordware Publishing, Inc., USA (428 pp).
Evans, S.G., Clague, J.J., 1994. Recent climatic change and catastrophic geomorphic processes in mountain environments. Geomorphology 10 (1–4), 107–128.
Fernández, P., Fornero, L., Maza, J., Rollan, R.A., Yánez, H., Núnez, M.S., de Alpeggiani, E.B., 1985. Hidrologıa del rıo Mendoza: simulación matemática del las hipótesis de rotura del dique natural formado por el Glaciar Grande del Nevado del Plomo y del traslado de las crecientes desde el glaciar hasta 200 metros aguas abajo de Alvarez Condarco. Instituto Nacional de Ciencia y Técnicas Hıdricas, Centro Regional Andino, Mendoza, Argentina.
Fernández, P.C., Fornero, L., Maza, J., Yañez, H., 1991. Simulation of flood waves from outburst of glacier-dammed lake. J. Hydraul. Eng. 117 (1), 42–53.
Fitzpatrick, A.A.W., Hubbard, A.L., Box, J.E., Quincey, D.J., Van As, D., Mikkelsen, A.P.B., ... Jones, G.A., 2014. A decade (2002–2012) of supraglacial lake volume estimates across Russell Glacier, West Greenland. Cryosphere 8 (1), 107–121.
Fountain, A.G., Walder, J.S., 1998. Water flow through temperate glaciers. Rev. Geophys. 36 (3), 299–328.
Gance, J., Malet, J.P., Dewez, T., Travelletti, J., 2014. Target detection and tracking of moving objects for characterizing landslide displacements from time-lapse terrestrial optical images. Eng. Geol. 172, 26–40.
Gleitsmann, L., Kappas, M., 2006. Glacier monitoring survey flights below clouds in Alaska: oblique aerial photography utilizing digital multiple image photogrammetry to cope with adverse weather. EARSel eProc 5 (1), 42–50.
Gulley, J., Benn, D.I., 2007. Structural control of englacial drainage systems in Himalayan debris-covered glaciers. J. Glaciol. 53 (182), 399–412.
Haeberli, W., 1983. Frequency and characteristics of glacier floods in the Swiss Alps. Ann. Glaciol. 4 (1), 85–90.
Harrison, W.D., Echelmeyer, K.A., Cosgrove, D.M., Raymond, C.F., 1992. The determination of glacier speed by timelapse photography under unfavourable conditions. J. Glaciol. 38 (129), 257–265.
Harrison, W.D., Osipova, G.B., Nosenko, G.A., Espizua, L., Kääb, A., Fischer, L., Huggel, C., Burns, P.A.C., Truffer, M., Lai, A.W., 2015. Glacier surges. In: Haeberli, W., Whiteman, C. (Eds.), Snow and Ice-related Hazards, Risks and Disasters. Elsevier, pp. 437–485.
Hashimoto, T., Kaneko, M., Rövid, A., Isono, S., Sone, T., Baba, K., Fukuda, A., Aniya, M., Naito, N., Enomoto, H., Skvarca, P., 2009. An introduction of high-precise 3D measurement system and its applications. J. Autom. Mob. Robot. Intel. Syst. 3, 4.
Hewitt, K., 1982. Natural dams and outburst floods of the Karakoram Himalaya. IAHS 138, 259–269.
Hewitt, K., Liu, J., 2010. Ice-dammed lakes and outburst floods, Karakoram Himalaya: historical perspectives on emerging threats. Phys. Geogr. 31 (6), 528–551.
Iribarren Anacona, P., Mackintosh, A., Norton, K.P., 2015. Hazardous processes and events from glacier and permafrost areas: lessons from the Chilean and Argentinean Andes. Earth Surf. Process. Landf. 40 (1), 2–21.
Irvine-Fynn, T.D., Sanz-Ablanedo, E., Rutter, N., Smith, M.W., Chandler, J.H., 2014. Measuring glacier surface roughness using plot-scale, close-range digital photogrammetry. J. Glaciol. 60 (223), 957–969.
Jacquet, J., McCoy, S.W., McGrath, D., Nimick, D.A., Fahey, M., O'kuinghttons, J., ... Leidich, J., 2017. Hydrologic and geomorphic changes resulting from episodic glacial lake outburst floods: Rio Colonia, Patagonia, Chile. Geophys. Res. Lett. 44 (2), 854–864.
Leiva, J.C., Lenzano, L.E., Cabrera, G.A., Suarez, J.A., 1989. Variations of Río Plomo Glaciers, Andes Centrales Argentinos. In: Glacier Fluctuations and Climatic Change. Springer, Netherlands, pp. 143–151.
Lenzano, M.G., Lannutti, E., Toth, C., Lenzano, L., Lo Vecchio, A., 2014. Assessment of ice-dam collapse by time-lapse photos at the Perito Moreno Glacier Argentina. Int. Arch. Photogramm. Remote. Sens. Spat. Inf. Sci. XL-1, 11–217. http://dx.doi.org/10.5194/isprsarchives-XL-1-211-2014.
Lenzano, M.G., Lannutti, E., Toth, C., Rivera, A., Lenzano, L., 2017. Detecting glacier surface motion by optical flow. Photogramm. Eng. Remote Sens. J (accepted on 10/26/2017).
Liss, C., 1970. Der morenogletscher in der patagonischen kordillere. Z. Gletscherk. Glazialgeol. VI (1-2), 161–180.
Lo Vecchio, A., Lenzano, M.G., Durand, M., Lannutti, E., Lenzano, L., Bruce, R., 2017. Estimation of speed motion and surface temperature from optical satellite imagery at Viedma glacier, Argentina. Glob. Planet. Chang (in review).
Loriaux, T., Casassa, G., 2013. Evolution of glacial lakes from the Northern Patagonia Icefield and terrestrial water storage in a sea-level rise context. Glob. Planet. Chang. 102, 33–40.
Maas, H.G., Casassa, G., Schneider, D., Schwalbe, E., Wendt, A., 2010. Photogrammetric determination of spatio-temporal velocity fields at Glaciar San Rafael in the Northern Patagonian Icefield. Cryosphere Discuss. 4, 2415–2432.
Margold, M., Jansson, K.N., Stroeven, A.P., Jansen, J.D., 2011. Glacial Lake Vitim, a 3000-km^3 outburst flood from Siberia to the Arctic Ocean. Quat. Res. 76 (3), 393–396.
Minowa, M., 2017. Frontal Ablation of Glaciar Perito Moreno, A Lake-terminating Glacier in Patagonia. (PhD Thesis, Course in Cryosphere Science Hokkaido University, 129 pp).
Minowa, M., Sugiyama, S., Sakakibara, D., Sawagaki, T., 2015. Contrasting glacier variations of Glaciar Perito Moreno and Glaciar Ameghino, Southern Patagonia Icefield. Ann. Glaciol. 56 (70), 26–32.
Minowa, M., Sugiyama, S., Sakakibara, D., Skvarca, P., 2017. Seasonal variations in ice-front position controlled by frontal ablation at Glaciar Perito Moreno, the Southern Patagonia Icefield. Front. Earth Sci. 5 (UNSP-1).
Narama, C., Duishonakunov, M., Kääb, A., Daiyrov, M., Abdrakhmatov, K., 2010. The 24 July 2008 outburst flood at the western Zyndan glacier lake and recent regional changes in glacier lakes of the Teskey Ala-Too range, Tien Shan, Kyrgyzstan. Nat. Hazards Earth Syst. Sci. 10 (4), 647–659.
Nuth, C., Kohler, J., König, M., Deschwanden, A.V., Hagen, J.O.M., Kääb, A., ... Pettersson, R., 2013. Decadal changes from a multi-temporal glacier inventory of Svalbard. Cryosphere 7 (5), 1603–1621.
Pasquini, A.I., Depetris, P.J., 2011. Southern patagonia's perito moreno glacier, Lake Argentino, and Santa Cruz River hydrological system: an overview. J. Hydrol. 405 (1), 48–56.
Pitkänen, T., Kajuutti, K., 2004. Close-range photogrammetry as a tool in glacier change detection. Int. Arch. Photogramm. Remote. Sens. Spat. Inf. Sci. 35, 769–773.
Richardson, S.D., Reynolds, J.M., 2000. An overview of glacial hazards in the Himalayas. Quat. Int. 65, 31–47.
Rivera, A., Corripio, J., Bravo, C., Cisternas, S., 2012. Glaciar Jorge Montt dynamics derived from photos obtained by fixed cameras and satellite image feature tracking. Ann. Glaciol. 53 (60), 147–155.
Rott, H., Stuefer, M., Siegel, A., Skvarca, P., Eckstaller, A., 1988. Mass fluxes and dynamics of Moreno Glacier, Southern Patagonia Icefield. Geophys. Res. Lett. 25 (9), 1407–1410.
Sersic, J.L., 1988. Ensayos sobre el glaciar Moreno. Academia Nacional de Ciencias, Argentina.
Skvarca, P., 2002. Importancia de los glaciares del hielo Patagónico Sur para el desarrollo regional. In: Haller, M.J. (Ed.), XV Congreso Geológico Argentino (El Calafate, 2002), Geología y Recursos Naturales de Santa Cruz. Relatorio V-1. pp. 1–14.
Skvarca, P., Naruse, R., 1997. Dynamic behavior of Glaciar Perito Moreno, southern Patagonia. Ann. Glaciol. 24, 268–271.
Skvarca, P., Naruse, R., 2005. Correspondence. Overview of the ice-dam formation and collapse of Glaciar Perito Moreno, southern Patagonia, in 2003/2004. J. Glaciol. 52 (177), 318–320.
Stuefer, M., 1999. Investigations on Mass Balance and Dynamics of Moreno Glacier Based on Field Measurements and Satellite Imagery. (PhD Thesis, Dissertation zur Erlangung des akademischen Grades eines Doktors der Naturwissenschaften an der Leopold-Franzens-Universitat Innsbruck, 163 pp).
Stuefer, M., Rott, H., Skvarca, P., 2007. Glaciar Perito Moreno, Patagonia: climate sensitivities and glacier characteristics preceding the 2003/04 and 2005/06 damming events. J. Glaciol. 53 (180), 3–16.
Sugiyama, S., Skvarca, P., Naito, N., Enomoto, H., Tsutaki, S., Tone, K., ... Aniya, M., 2011. Ice speed of a calving glacier modulated by small fluctuations in basal water pressure. Nat. Geosci. 4 (9), 597–600.
Svanem, M., 2010. Terrestrial Photogrammetry for Velocity Measurement of Kronebreen Calving Front. Norwegian University of Life Sciences (Master's Thesis, 94 pp).
Toth, C., Jóźków, G., 2016. Remote sensing platforms and sensors: a survey. Int. J. Photogramm. Remote Sens. 115, 22–36.
Tweed, F.S., Russell, A.J., 1999. Controls on the formation and sudden drainage of glacier-impounded lakes: implications for jökulhlaup characteristics. Prog. Phys. Geogr. 23 (1), 79–110.
Vincent, C., Auclair, S., Meur, E.L., 2010. Outburst flood hazard for glacier-dammed Lac de Rochemelon, France. J. Glaciol. 56 (195), 91–100.
Walder, J.S., Costa, J.E., 1996. Outburst floods from glacier-dammed lakes: the effect of mode of lake drainage on flood magnitude. Earth Surf. Process. Landf. 21 (8), 701–723.
Westoby, M.J., Glasser, N.F., Brasington, J., Hambrey, M.J., Quincey, D.J., Reynolds, J.M., 2014. Modelling outburst floods from moraine-dammed glacial lakes. Earth Sci. Rev. 134, 137–159.